JPhys Materials

TOPICAL REVIEW • OPEN ACCESS

Pulsed laser deposition of oxide and metallic thin films by means of Nd:YAG laser source operating at its 1st harmonics: recent approaches and advances

To cite this article: S K Chaluvadi *et al* 2021 *J. Phys. Mater.* **4** 032001

Journal of Physics: Materials

RECEIVED
2 November 2020

REVISED
28 January 2021

ACCEPTED FOR PUBLICATION
15 February 2021

PUBLISHED
14 April 2021

TOPICAL REVIEW

Pulsed laser deposition of oxide and metallic thin films by means of Nd:YAG laser source operating at its 1st harmonics: recent approaches and advances

S K Chaluvadi[1], D Mondal[1,2], C Bigi[1], D Knez[1], P Rajak[1,2], R Ciancio[1], J Fujii[1], G Panaccione[1], I Vobornik[1], G Rossi[1,3] and P Orgiani[1,4]

[1] CNR-IOM, TASC Laboratory in Area Science Park, 34139 Trieste, Italy
[2] International Centre for Theoretical Physics (ICTP), 34100 Trieste, Italy
[3] Department of Physics, University of Milano, 20133 Milano, Italy
[4] CNR-SPIN, UOS Salerno, 84084 Fisciano, SA, Italy

E-mail: pasquale.orgiani@spin.cnr.it

Keywords: pulsed laser deposition, thin films, XRD, STM, ARPES

Abstract

Quantum materials are central for the development of novel functional systems that are often based on interface specific phenomena. Fabricating controlled interfaces between quantum materials requires adopting a flexible growth technique capable to synthesize different materials within a single-run deposition process with high control of structure, stoichiometry, and termination. Among the various available thin film growth technologies, pulsed laser deposition (PLD) allows controlling the growth of diverse materials at the level of single atomic layers. In PLD the atomic species are supplied through an ablation process of a stoichiometric target either in form of polycrystalline powders or of a single crystal. No carrier gases are needed in the deposition process. The ablation process is compatible with a wide range of background pressure. We present results of thin-film growth by PLD obtained by using an Nd:YAG infrared pulsed laser source operating at its first harmonics. With respect to the traditional PLD systems—based on excimer KrF UV-lasers—optimal conditions for the growth of thin films and heterostructures are reached at large target-to-substrate distance. Merits and limitations of this approach for growing oxide and non-oxide thin films are discussed. The merits of an Nd:YAG laser to grow very high-quality thin films suggest the possibility of implementing compact *in-situ* setups e.g. integrated with analytical instrumentation under ultra-high vacuum conditions.

1. Introduction

Quantum materials exhibit unique physical phenomena at their surfaces, especially if grown in ultra-thin films with epitaxial strain induced by the substrate or by the interface in heterostructures with other functional materials [1–4]. In this respect, the thin film technology is currently able to go beyond the single-crystals technology. In particular, this allows the investigation of physical properties in the limit of single atomic layers, through the controlled deformation of the structural parameters by substrate induced strain and growth of multi-layers, providing key information for the development of real layered device applications [3–5]. It therefore stems from the need to use flexible growth techniques capable of synthesising a large variety of functional materials within the same dedicated apparatus. In this respect, even though molecular beam epitaxy (MBE) has been widely used for decades to grow very high quality thin and ultra-thin films and multilayers, strong limitations arise on the compatibility of diverse materials (e.g. transition metals and rare earths) within the same ultra-high vacuum (UHV)-system, due to possible cross-contamination. On the contrary, pulsed laser deposition (PLD) is known to be a very versatile tool with several great flexibility in the choice of materials to grow, easy tunability in the film growth rate, and full suitability for growing heterostructures and the control of volatile elements [6, 7]. In a PLD system, the single

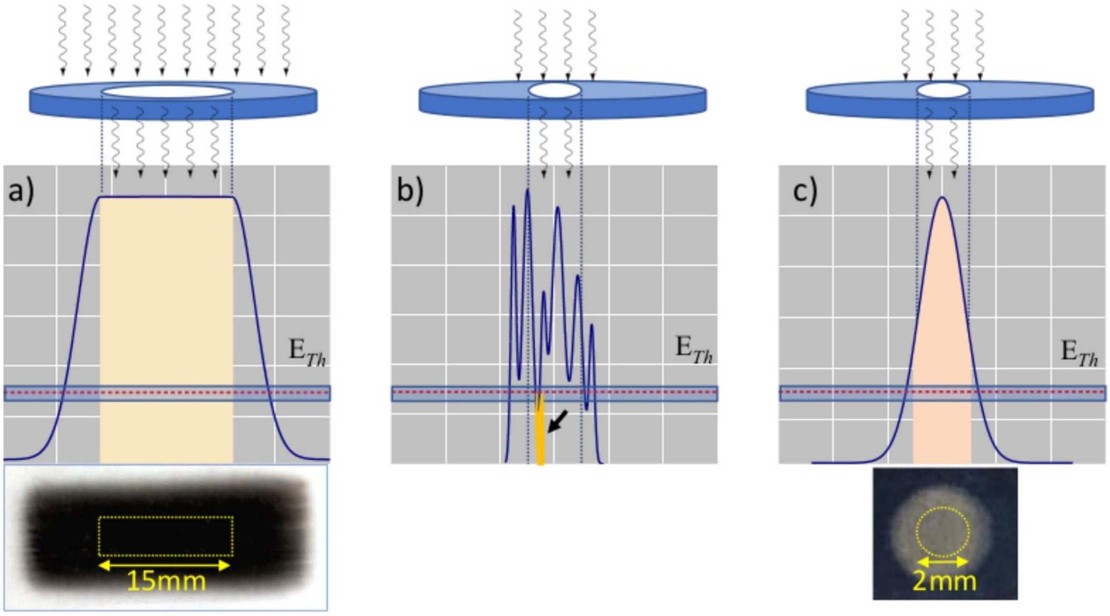

Figure 1. Typical energy profile of a KrF excimer (a), an early-stage (b) and a new-generation state-of-the-art (c) Nd:YAG lasers, respectively; for all of the laser spot, the effect of using a shadow-mask (blue) to tentatively improve the uniformity of the energy profile is shown; threshold energy E_{Th} (red dotted line) is also reported; in particular, in the case of the inhomogeneous laser beam (b), sub-threshold region (yellow) is enlightened by a black arrow. Energy profiles obtained by thermal paper at the output of the laser window are also reported for a KrF (a) and a state-of-the-art Nd:YAG (c) lasers, respectively.

atomic species of complex materials are supplied through an ablation process of a target—in form of poly-crystalline powders and/or single crystal—by the irradiation of a focused highly intense pulsed laser beam impinging onto the target at an angle of 45° or 60° [8, 9] from the surface normal. Multi-layered heterostructures can be easily engineered by positioning alternate the different targets in the laser focus, in a continuous vacuum condition [10, 11]. PLD shares with other deposition techniques the high cleanness of the growth environment which prevents contamination, as well as the extremely low deposition rate achievable during the growth (down to 0.01 nm s^{-1}). Moreover, since the propagation of the plume of ablated materials is inhibited only at very high background pressure (i.e. several mbar), deposition processes at such a high partial pressure are indeed possible. Such a capability is particularly important during the growth of materials containing highly volatile elements (e.g. oxygen, selenium), whose re-evaporation rate can be reduced by increasing the background pressure.

Most of the PLD systems are routinely equipped with a KrF excimer pulsed laser source ($\lambda = 248$ nm), where the laser pulses are produced by an electrical discharge within a gaseous mixture of the halogen F and the noble Kr gases in a buffer gas made of Ne. As the product of ionization of Kr ions into Kr^+, a metastable KrF dimer is created with a characteristic lifetime of tens of nanoseconds, which chemical dissociation produces photons in the ultra-violet (UV) range. The typical spot size of a KrF laser pulse is about 3 cm^2 while their energy range from 300 to 700 mJ (panel (a) in figure 1) [12]. Laser pulses are subsequently focused on targets with a typical energy density of about 2–3 J cm^{-2}. Even though excimer lasers are widely used in PLD laboratories worldwide, safety issues (e.g. presence of highly poisoning F gas) can limit their dissemination, e.g. in users facilities.

An alternative strategy based on the use of solid state lasers has emerged. In particular, considerable activity has been dedicated to Nd:YAG lasers in which an Nd-doped $Y_3Al_5O_{12}$ Yttrium Aluminum Garnet rod is optically pumped by a Krypton flash tube. One of the most important characteristics of such a laser source is nowadays the high energy output of the fundamental harmonics emitting in the Infra-Red (IR) region at 1064 nm (i.e. up to 1–2 J). The typical spot size of a Nd:YAG laser pulse is 5–6 mm diameter wide, corresponding to an energy density of 3–4 J cm^{-2} for an unfocused beam. Such an energy per laser pulse is so intense that Nd:YAG lasers are capable to ablate materials without need of focusing on target. Moreover higher harmonics radiation can be generated with suitable crystal converters, reaching the UV range (e.g. fourth and fifth harmonics emitting at 266 nm and 213 nm, respectively) [13]. Yet, until the last decade [12], the spatial uniformity of the laser beam energy has raised concerns for their application in PLD.

In the PLD growth technique, the ablation process (i.e. a solid-vapor transition of the target) is characterized by a threshold energy E_{Th} which depends on the material [8, 9]. When the laser pulse energy is well above E_{Th}, it mostly result into a congruent ablation of the target and the obtained films do not show any sign of clusters/droplets. However, for the laser pulses whose energy lies in proximity of the E_{Th} value, spurious phases in submicron areas, precipitates and structural defects can be produced [14]. In this respect, excimer lasers generate highly uniform laser pulses [12] whose energy profile can be further improved by using an optical mask to remove the peripheral region of the beam (panel (a) in figure 1). On the other hands the early-stage Nd:YAG lasers systematically led to the presence of small droplets embedded in the grown films. The droplets have been associated to the spatial inhomogeneity of the laser beam produced by the Nd:YAG rod (panel (b) in figure 1) thus limiting in fact their use in the growth of high quality thin films [12]. In the last decade, however, a considerable effort has been spent in optimizing the spatial profile of the laser pulse's energy beam, which nowadays shows similar characteristic with respect to the laser beam produced by an excimer laser (panel (c) in figure 1).

By taking the advantage of the new generation Nd:YAG laser source, here, we report on the progress on PLD grown thin films by using such source as integrated as alternative source to KrF in the UHV PLD system of the NFFA user facility in Trieste [15]. Instead of following the traditional usage of higher harmonics of Nd:YAG lasers, we show that, by using the fundamental wavelength, the congruent ablation of both metallic (i.e. iron selenide FeSe) and insulating (i.e. titanium dioxide TiO_2) targets can be successfully achieved. Unexpectedly, the IR-radiation of the fundamental harmonics of Nd:YAG lasers at 1064 nm—corresponding to impinging photons with energy of about 1.16 eV—is proved to be efficiently absorbed by insulating materials characterized by large value of the band-gap (e.g. 3.4 eV for anatase TiO_2). Even though a large number of oxide materials are known to show metallic surface states upon a continuous irradiation in UHV condition, the ablation process of TiO_2 (as well as other oxide materials such as CeO_2, $LaAlO_3$, $SrTiO_3$) immediately starts since the very first laser shots. Rather than the presence of a conducting layer at their surface, the absorption of IR-radiation might be correlated to the formation of in-gap states (i.e. 0.5–1.5 eV from Fermi's edge). As a matter of fact, even a very small amount of oxygen deficiency has been proved to create localized states within the band gap [16–19] and their occurrence might very effectively explain how a 1.16 eV can be absorbed and produces its ablation. Finally, by fine tuning the target-to-substrate distance, droplets free thin films with improved surface structural properties can be obtained.

By exploiting the full output energy of the Nd:YAG laser sources, the ablation of materials characterized by an extremely high E_{Th} is therefore possible. By increasing the target-to-substrate distance, beam-assisted growth diagnostics can rely on higher incident angles; similarly, time-of-flight based techniques investigating the plume dynamics would be further refined by the increased target-to-substrate distance [20]. Finally, the use of the fundamental emission line further simplifies the setup.

2. Experimental

PLD growth of epitaxial FeSe and TiO_2 thin films was performed using a Innolas Spitlight Compact 400–10 Nd:YAG pulsed laser source by means of its first harmonics at 1064 nm at the NFFA-APE facility of IOM-CNR and Elettra in Trieste [15]. The pristine spot-size of the laser shot was about 5 mm in diameter with a typical energy of 700 mJ, corresponding to an energy density of about 3.5 J cm^{-2} for the unfocused beam. With the dual aim of avoiding the peripheral region of the laser spots as well as reducing the growth rate per laser shot, an optical mask was used to reduce the spot-size from 5 to 2 mm in diameter. Laser pulses were therefore focused on a stoichiometric polycrystalline FeSe target (purity 99.99%) and on a rutile TiO_2 single crystal. The laser repetition rate was varied from 10 Hz down to 0.1 Hz. Epitaxial growth of FeSe and TiO_2 thin films was performed under UHV conditions (i.e. base pressure in the range of 10^{-8} mbar) and in 10^{-4} mbar ultra-pure oxygen background atmosphere (purity at 99.9999%), respectively. The substrate-to-target distance d was also varied from 5 to 10 cm. After the film growth, the samples were cooled down to room temperature in about 15 minutes at the same background pressure deposition condition. Structural characterization of the as-grown films was carried out *ex-situ* using a four-circle Panalytical X'pert diffractometer with a Cu K_α radiation source. Chemical composition of the FeSe grown samples were determined also *ex-situ* by energy dispersive spectroscopy (EDS) experiments carried out by Oxford LN_2-free X-Act Silicon Drift Detector and calculated by Aztec software. The atomic structure of the films was investigated in cross-section by high-resolution transmission electron microscopy (HRTEM) and selected area electron diffraction (SAED). Cross-sectional TEM samples were prepared with a conventional polishing technique followed by dimpling and milling with Ar ions. HRTEM experiments were performed using a JEOL 2010 UHR TEM equipped with a field emission gun and operated at 200 kV. Microscopy data analysis was performed with the Gatan Microscopy Suite 3.20.1314.0 (GMS). The surface morphology of both FeSe and TiO_2 was investigated *in-situ*, under UHV conditions, by atomic-resolution scanning tunnel microscopy (STM) at the NFFA-APE-IOM beamline at the Elettra synchrotron facility. The surface long range order was also probed *in-situ* by low-energy electron diffraction (LEED). Finally, the electronic states at the surfaces of selected samples were investigated by *in-situ* angle-resolved photo-emission spectroscopy (ARPES) with

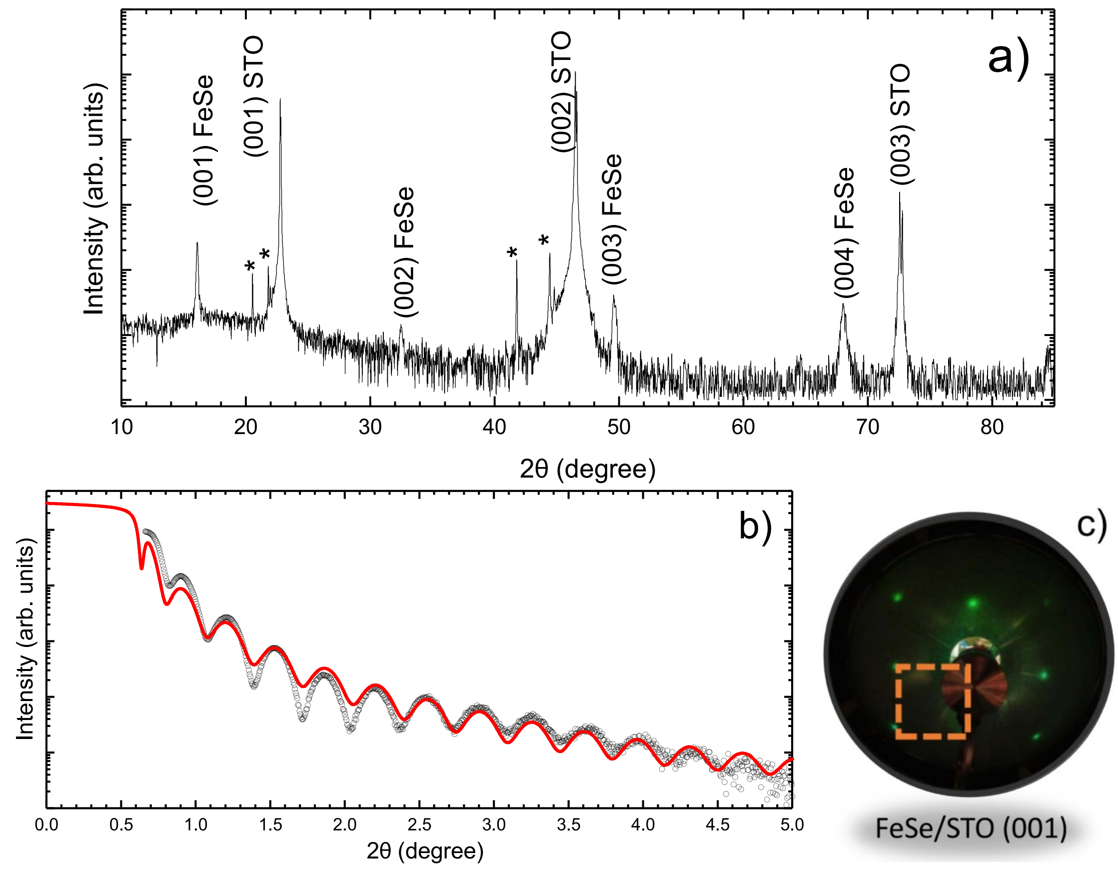

Figure 2. (a) Symmetrical $\theta - 2\theta$ and (b) low-angle x-ray reflectivity scans of a FeSe thin film grown on STO (001) substrate (simulation of low-angle x-ray reflectivity is also reported as red solid line); (c) typical LEED pattern of FeSe showing the 1 × 1 surface reconstruction.

synchrotron radiation (APE-LE beamline) and a Scienta DA30 hemispherical electron energy and momentum analyzer which allows performing the band mapping over the extended areas of the Brillouin zone without sample rotation. The overall energy resolution was set to 100 meV, and the angular resolution was set to 0.2°.

3. Growth and characterization of iron selenide FeSe

Iron selenide FeSe has recently attracted a great interest because of the complex electronic phase diagram shown as a function of temperature [21–25]. FeSe undergoes structural transition from tetragonal to orthorhombic about 90 K. At intermediate temperatures (i.e. $100\ \mathrm{K} < T < 300\ \mathrm{K}$), a nematic state—namely an electronic order that breaks the rotational symmetries without changing the translational symmetry of the lattice—has been observed [26]. More interestingly, at lower temperatures (i.e. below 8 K), it finally becomes superconducting [21]. Even though several reports on FeSe thin films indicate that the superconducting critical T_c can be tuned by the substrate induced epitaxial strain [27, 28] other works point to the electronic interfacial coupling between film and substrate to interpret such a T_c enhancement in ultra-thin films [29, 30]. It is, therefore, necessary to have access to high-quality single-crystalline FeSe ultra-thin films, for both fundamental studies as well as to develop potential quantum devices.

From the structural point of view, FeSe has a simple quasi-two-dimensional crystal structure (i.e. Fe lattice sandwiched between two adjacent Se layers) with space group belonging to P4/nmm [31]. The in-plane a and the out-of-plane c lattice parameters are 0.377233 nm and 0.552249 nm, respectively. Despite the large in-plane lattice mismatch with (001) $SrTiO_3$ (STO) showing a lattice parameter of 0.3905 nm (thus corresponding to about −3.5% tensile strain), many experiments on FeSe thin and ultra-thin (i.e. single monolayer) films have been reported when grown on this specific substrate due to the very high superconducting critical temperature here observed [28, 29].

Differently from other selenides [32, 33], FeSe thin films were grown in UHV condition with the expected Fe:Se = 1:1 chemical ratio as confirmed by EDS experiments. The growth parameters were initially optimized by monitoring the structural properties of the thin films. Symmetrical $\theta - 2\theta$ scan (panel (a) in

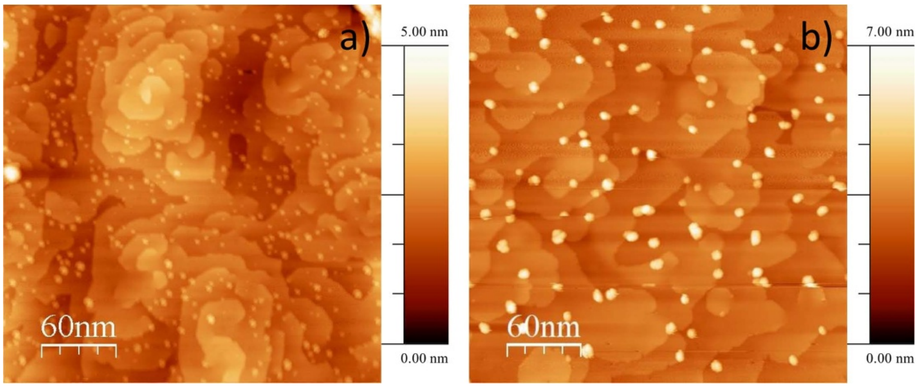

Figure 3. STM topography images of FeSe thin films grown at 420 °C and the substrate-to-target distance of about 5 cm (a) and 10 cm (b), respectively.

figure 2) of a FeSe film grown at 420 °C on a (001) STO substrate shows only the (00*l*) diffraction peaks thus indicating the preferential *c*-axis growth direction, without any trace of secondary phases or other crystallographic orientation. The out-of-plane lattice parameter *c*, determined from the FeSe (001) diffraction peak, was calculated to be approximately 0.551 nm, which is equal with the values reported for the relaxed films. FeSe film thickness and its surface roughness were then investigated by low-angle x-ray reflectivity (XRR), as shown in panels (b) in figure 2. Simulations of the low-angle XRR (red curve in panel (b) in figure 2), performed by means of the IMD package of XOP software [34] (red curve in panel (b) in figure 2) fully matched the design value of 25 nm. XRR oscillations were recorded up to 2θ values of about 5°, while, above this angle, the oscillations fell below the experimental sensitivity of the x-ray diffractometer, thus inferring a very low surface roughness. Finally, *in-situ* LEED experiments measured at the electronic kinetic energy of 100 eV (panel (c) in figure 2) did show sharp diffraction spots arranged in a square-geometry with no sign of surface reconstruction.

To gain further insights regarding the surface structural order of the FeSe films, *in-situ* STM experiments—using an atomic resolution ultrahigh vacuum (UHV-STM) apparatus at room temperature—were also performed. Even though FeSe films exhibited very good structural features—as proved by the combination of XRD, XRR and LEED—a consistent number of spirals and nm-wide droplets were observed by means of STM (panel (a) in figure 3). These droplets were distributed uniformly on the film surface without any preferential positions. It is noteworthy to underline that the very presence of such droplets is somehow commonly observed in thin films grown by Nd:YAG-based PLD [35].

In order to reduce the number of spirals as well as the density of droplets in the film, FeSe films were therefore grown by substantially increasing the substrate-to-target distance *d* up to about 10 cm. As a matter of fact, at this deposition condition (i.e. 10^{-8} mbar), the expected mean free path for the ablated single atoms from the PLD target is larger than the used substrate-to-target distance while the probability of large clusters to reach the substrate may be reduced. Accordingly, the amount of materials condensing onto the substrate surface should simply scale with the solid angle (i.e. $\sim d^2$) therefore further reducing the growth rate without affecting the Fe:Se chemical ratio. As shown in panel (b) in figure 3, the STM topography image revealed atomically flat terraces along with a sizable reduction (i.e. 70%) of droplets. Moreover, differently from the film grown with smaller substrate-to-target distance *d*, the remaining droplets are no longer randomly distributed over the entire film surface but appear concentrated at the edges of the film's terraces. Therefore, to further reduce the possible number of nucleation sites for the droplets, the deposition temperature was slightly increased from 420 °C to 450 °C and to 470 °C (panels (a), (b) and (c) in figure 4, respectively).

The average terrace widths measured along the white solid line on the film surface was about 20–30 nm for the FeSe film grown at 420 °C (panels (a) and (e) in figure 4), whereas, by increasing the substrate deposition temperature to 450 °C, the terrace widths have been increased up to 80 nm (panels (b) and (f) in figure 4). As expected, the higher thermal mobility of ad-atoms onto the film surface favored the formation of wider terraces to which corresponded a reduction of droplets on the surface of the film. A further increase of the deposition temperature (i.e. 470 °C), however, reduced the number of droplets, yet the average width of film terraces was slightly reduced from 80 to 60 nm (panels (c) and (g) in figure 4). Irrespective of the substrate deposition temperature, the average height of the droplets measured was about 2–3 nm and the root mean square (RMS) roughness values of all the films lie below 0.5 nm i.e. one unit cell height of FeSe. Even though the droplets on the film surface were extremely reduced in number, the formation of droplets at any deposition conditions (e.g. temperature of substrates, growth rate) might indicate that a residual spatial

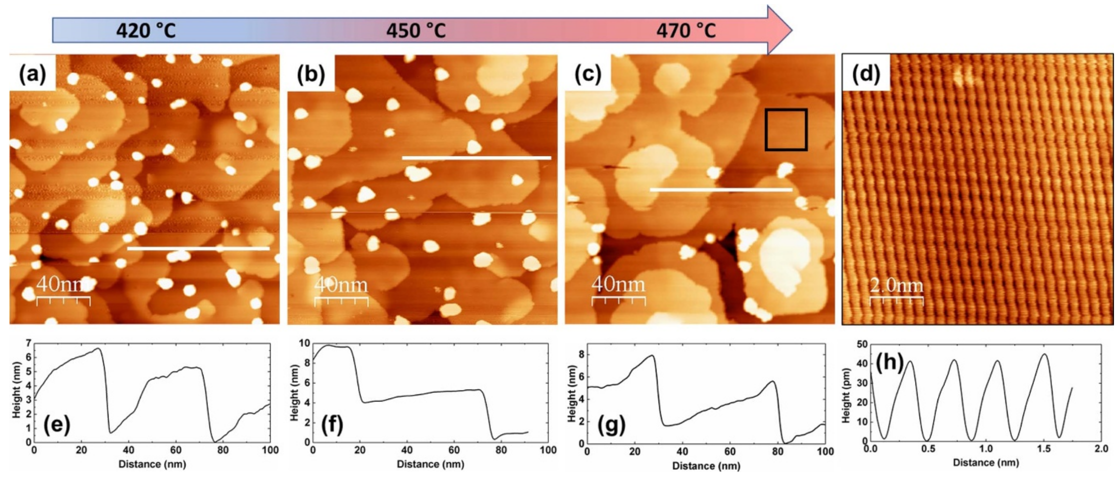

Figure 4. STM topography images of FeSe thin films grown at substrate-to-target distance of 10 cm and at different temperatures (namely 420 °C (a), 450 °C (b) and 470 °C (c), respectively, in the scan area of 200 × 200 nm^2). The atomic resolution of the zoomed area marked as the black box in (c) in the scan area of 12 × 12 nm^2. The corresponding line-profiles of all the samples are shown in (e)–(h) graphs.

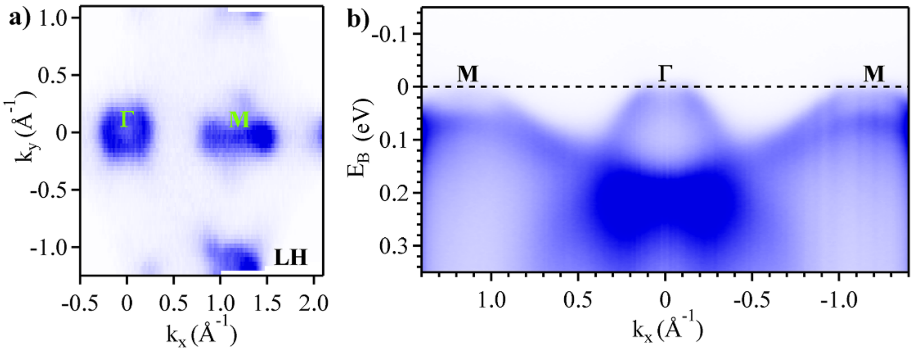

Figure 5. ARPES map at Fermi (a) and valence band spectra measured along Γ-M direction (b) of FeSe film measured using horizontally polarized light of 85 eV excitation energy, respectively.

inhomogeneity in the laser beam energy profile is still present in the new generation ND:YAG lasers. Nevertheless, STM topography of FeSe films did show a substantial absence of those droplets and always showed the atomically resolved Fe arrangement (panel (d) in figure 4). It is crucial to underline that both the structural as well as the electronic properties probed by XRD and resistivity measurements (always ranging from 200 to 400 $\mu\Omega$ cm at room temperature) were not able to reveal sizable differences among the FeSe samples, being them more sensitive to the bulk of the materials. This result paves the way for identifying the correct experimental conditions to optimize the surface of the film with respect to the number of droplets or width of terraces.

In order to ascertain the correlation between the structural and physical properties of PLD-grown FeSe thin films (e.g. the residual presence of droplets), in ARPES experiments were performed. The high surface sensitivity of ARPES at UV and soft-X ray energies and the direct mapping of electron band dispersion provide the best test of quality of the film's surface (e.g. surface roughness, presence and extension of undesired spurious phases) [36–38]. Similar to STM investigations, ARPES experiments were carried out on the freshly grown FeSe samples transferred *in-situ* from PLD growth chamber directly under UHV ($<10^{-10}$ mbar). The Fermi surface and the band dispersion along Γ-M high symmetry direction of a FeSe film measured by ARPES technique at 45 K temperature and with a linearly polarized (horizontal -HP) photon beam of energy of 85 eV are shown in panels (a) and (b) in figure 5, respectively.

The Fermi surface measured with HP light (panel (a) in figure 5) displays elliptical shape along k_x at Γ-point and flower-shaped with four lobes centered at the M-point of the Brillouin zone, respectively. Consistently, the valence band spectra taken along the Γ-M high symmetry direction shows Fe t_{2g} derived hole-like band at the Γ-point, which creates the elliptical shape of the Fermi surface [38]. At the M point of the valence band (panel (b) in figure 5), two electron-like and two hole-like bands which are again derived

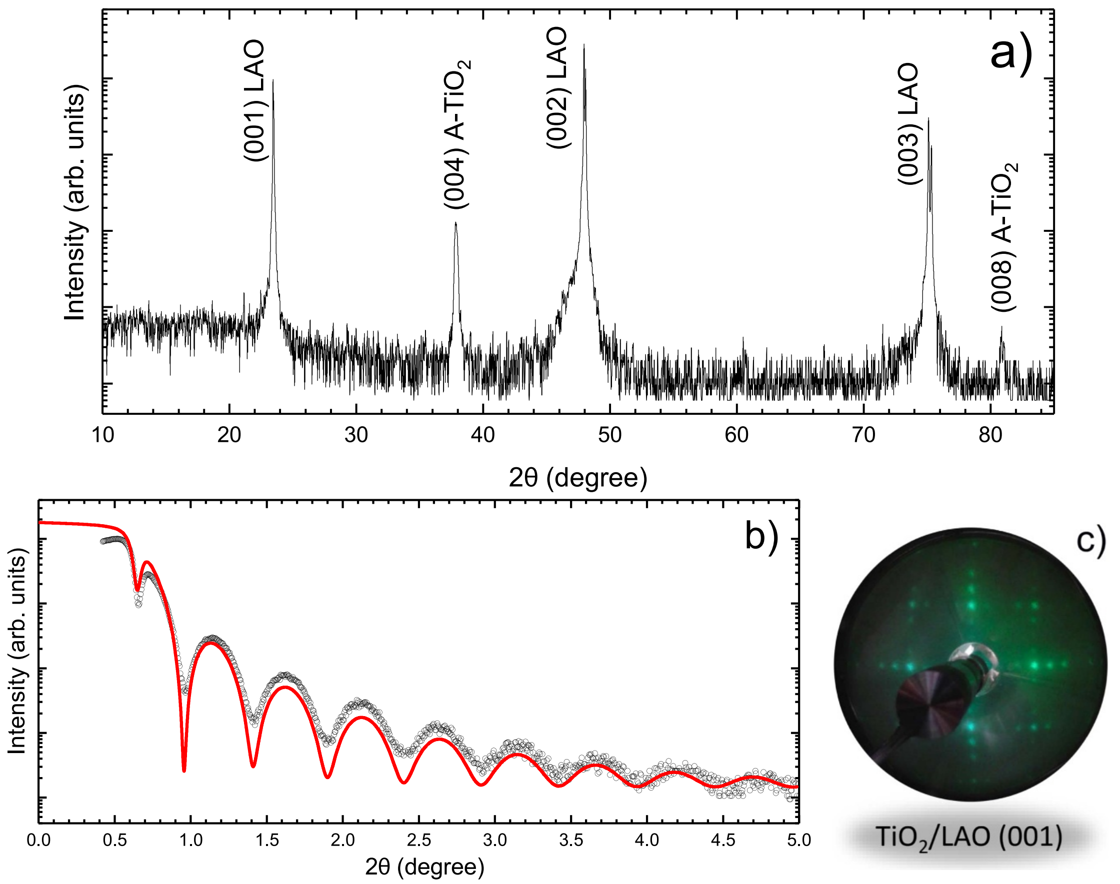

Figure 6. (a) Symmetrical $\theta-2\theta$ and (b) low-angle x-ray reflectivity scans of an anatase TiO_2 film grown on $LaAlO_3$ (001) substrate (simulation of low-angle x-ray reflectivity is also reported as red solid line); (c) typical LEED pattern of TiO_2 showing the (4 × 1)–(1 × 4) surface reconstruction.

from the Fe t_{2g} states were observed, form the earlier described flower-shaped pockets at the Fermi surface [38]. The overall observed ARPES features are in very good agreement with the ones measured on cleaved single crystals [39] and thin films grown by MBE [28, 29], thus demonstrating the very high structural quality of FeSe thin films grown by PLD using the fundamental harmonics of Nd:YAG laser.

4. Growth and characterization of anatase titanium dioxide TiO_2

Differently for the PLD-growth of highly metallic targets (e.g. FeSe), the use of Nd:YAG pulsed laser sources for insulating targets—such as oxide materials—is less commonly used. Oxide thin films are usually deposited by means of UV-radiation produced by excimer lasers [11, 40–43], resulting in very high quality of the surface and structural properties [17, 44–46]. Reports show that the use of Nd:YAG laser source for the growth of oxide thin films is mostly confined to its higher (from second to fifth) harmonics [13, 47, 48] and the wavelength falling in UV-range. However, we here show that very high quality oxide thin films can be also obtained by using the fundamental emission of Nd:YAG laser with wavelength falling in the IR-region at 1064 nm. In particular, we will exploit the possibility of using such a laser source in growing epitaxial thin film of anatase titanium dioxide TiO_2 which is among the most investigated oxide material for possible applications in photo-catalysis, quantum electronics and many other fields. Epitaxial anatase TiO_2 thin films were grown on (001)-oriented $LaAlO_3$ (LAO) substrate at 700 °C under 10^{-4} mbar of oxygen background pressure. Similarly to the previous case, the crystallographic properties of the films, as well as their surface long range order, were probed by *ex-situ* XRD and XRR and *in-situ* LEED

The symmetrical θ–2θ XRD scan (panel (a) in figure 6) only contains anatase diffraction peaks, indicating that the sample was single phase and well oriented, with the possible occurrence of secondary phases or other crystallographic orientations below the accuracy of the measurement. Surface roughness of the film was therefore probed by low-angle XRR (panel (b) in figure 6) and evaluated by numerical simulations performed by means of the IMD package in the XOP software (red curve in panel (b) in figure 6) [34]. Similar to the FeSe case, XRR oscillations were recorded up to 2θ values above 5° when eventually they

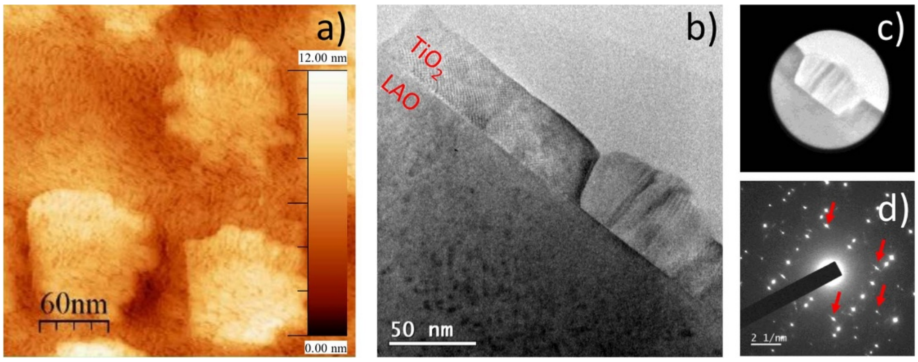

Figure 7. (a) STM topography image of a TiO_2 thin film grown at substrate-to-target distance of about 5 cm; (b) cross-sectional HRTEM of the same films in the proximity of the flower-shaped structure; (c)–(d) SAED of a flower-shaped domain (red arrows correspond to diffraction spots associated to the rutile phase).

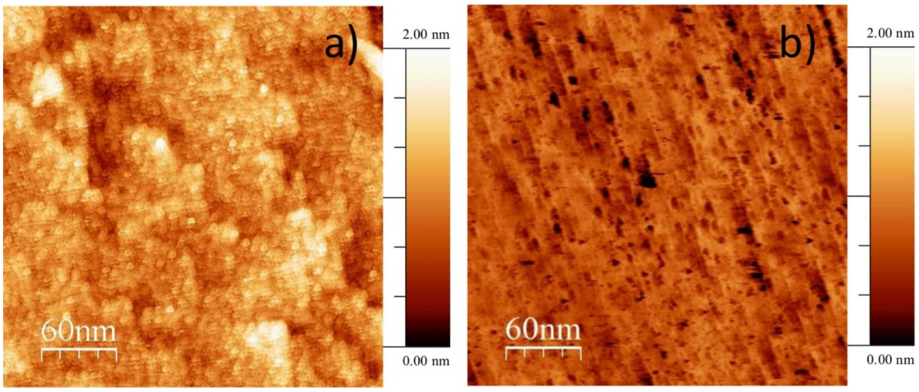

Figure 8. STM topography images of a TiO_2 thin film grown by first harmonics Nd:YAG laser at substrate-to-target distance of about 10 cm (a) and by KrF laser at substrate-to-target distance of about 5 cm (b), respectively.

fell below the experimental sensitivity of the x-ray diffractometer. The crystal quality of the films extends up to the surface, as confirmed by LEED $(4 \times 1)-(1 \times 4)$ surface reconstruction in the panel (c) in figure 6. The ensemble of these data clearly does not reveal any substantial differences between the TiO_2 thin films grown by either the excimer UV-radiation [17] or the Nd:YAG IR-radiation.

To gain insights on the structural features of TiO_2 thin films at nano and sub-nano scales, *in-situ* STM experiments were also performed in the scan area of $300 \times 300\ \mathrm{nm}^2$. Similarly to the previous case, the experiments were performed *in-situ* immediately after the growth of the samples. Differently from the FeSe case, in which nano-meter droplets were observed over the entire surface of the film, the STM topography of a TiO_2 film—grown at typical target-to-substrate distance d of about 5 cm—did not show any sign of droplets. However, much larger (i.e. 80 nm) flower-shaped structures embedded in the atomically flat film (panel (a) in figure 7) were observed. In order to understand the nature of such flower-shaped structures, we performed HRTEM experiments (panels (b)–(d) in figure 7). Cross-sectional HRTEM revealed that the large part of the TiO_2 film shows the typical modulated structure associated with the occurrence of oxygen vacancies, self-organizing into regular arrays of planar defects [44, 49–51]. In addition, SAED experiments (panels (c) and (d) in figure 7, respectively) indicated that the poly-crystalline nature of those flower-shaped structures corresponds to rutile clusters embedded into the anatase matrix.

The evidence that the thickness of both the film and the flower-shaped structures appear to be identical and their crystalline nature is not compatible with a droplet formation taking place during the ablation process [35]. However, such rutile clusters might be related to the growth of spurious phases nucleated from nanometer-sized droplets at the very beginning of the film growth. Therefore, similarly to the FeSe case, with the aim of reducing the possible occurrence of droplets as well as the growth rate of the TiO_2 films, the substrate-to-target distance d was increased up to about 10 cm. As a matter of fact, even at O_2 background pressure of 10^{-4} mbar, the expected mean free path of ablated single atoms is larger than the substrate-to-target distance while it could be smaller for ablated large cluster of material. As shown in panel (a) in figure 8, STM topography image revealed that the TiO_2 thin films did grow with atomically flat

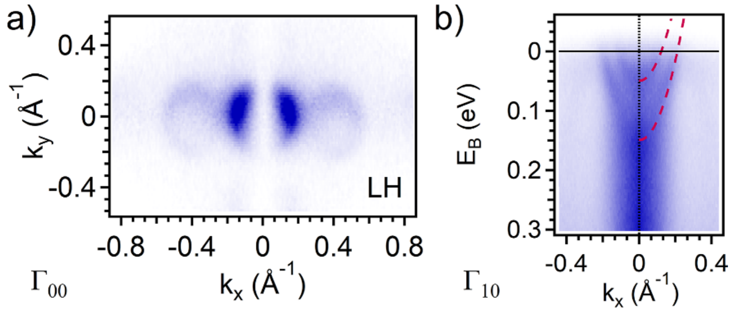

Figure 9. ARPES map at Fermi (a) and energy dispersion at center of the second Brillouin zone (b) of the annealed sample of a TiO_2 film measured with a photon energy of 46 eV with HP of the light, respectively. The parabolic dispersion of the 2DEG is enlightened by red dotted curves.

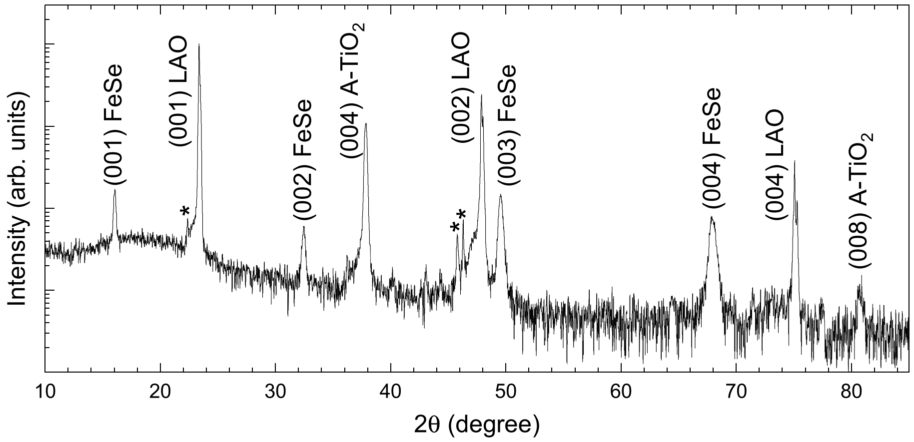

Figure 10. Symmetrical $\theta-2\theta$ scan of a $FeSe/TiO_2$ bilayered film grown on LAO substrate (asterisks are due to the characteristic wavelengths of the unmonochromatized x-ray source).

termination with no trace of neither droplets nor flower-shaped rutile poly-crystalline domains (panel (a) in figure 8). Such a result confirms that TiO_2 thin films grown by 1st harmonics of Nd:YAG laser is structurally equivalent to those grown by excimer lasers (panel (b) in figure 8).

Similarly to the previous case, the electronic properties of the TiO_2 films grown by first harmonics Nd:YAG was investigated at their surface by *in-situ* ARPES experiments thus providing a indirect probe of its structural quality. As reported in literature [48, 52], we have observed a two dimensional electron gas (2DEG) laterally modulated by the $(4 \times 1)-(1 \times 4)$ surface reconstruction occurred at (001) surface of anatase TiO_2 thin films (figure 9). These ARPES features are in very good agreement with the ones measured on epitaxial anatase TiO_2 thin films grown by means of excimer as well as fifth harmonics of Nd:YAG lasers.

5. Growth and characterization of $FeSe/TiO_2$ bi-layers

With the final aim to show the high flexibility of the PLD over other growth techniques, heterostructures based on metallic non-oxide FeSe and insulating oxide TiO_2 constituent layers were grown. By taking advantage of the similarities between the crystal structure of FeSe and TiO_2, $FeSe/TiO_2$ bi-layers were therefore grown on (100) oriented LAO substrates. Accordingly to the optimized growth parameters for the single layers, the target-to-substrate distance *d* was set at about 10 cm. TiO_2 layer was deposited at high temperature (i.e. 700 °C) and at 10^{-4} mbar of oxygen pressure, while the FeSe layer was deposited at lower temperature (i.e. 450 °C) and in UHV condition (i.e. $<10^{-7}$ mbar). As expected, *ex-situ* structural characterizations by XRD only showed the (00*l*) diffraction peaks for both TiO_2 and FeSe thus demonstrating the preferential orientation along the [001] direction (figure 10).

Similarly to the previous cases, surface long range order and roughness were investigated by *in-situ* LEED and STM, respectively (figure 11). As expected, similarly to FeSe thin films directly grown on single-crystal substrates, LEED pattern did show the simple 1 × 1 surface reconstruction of FeSe layer grown on top of a TiO_2 thin film. Moreover, the STM topography image measured in the scan area of 300×300 nm^2 (panel (b)

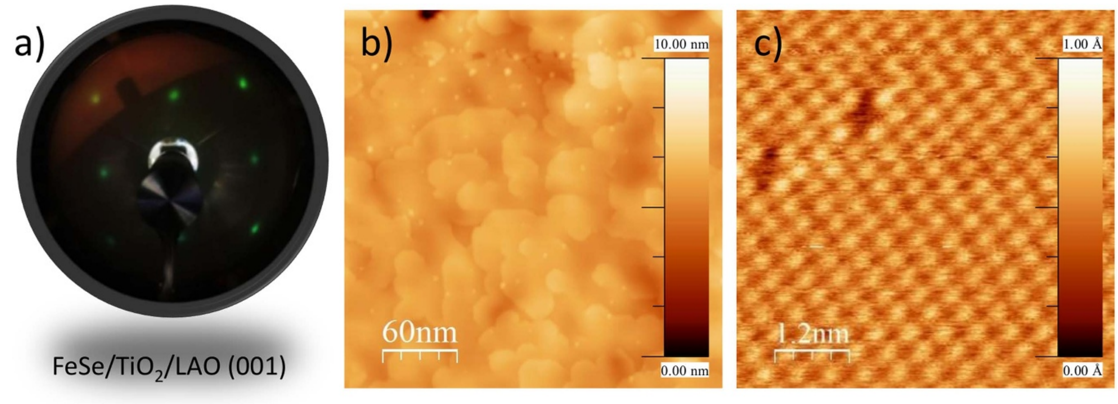

Figure 11. (a) LEED pattern showing the FeSe 1 × 1 surface reconstruction and STM topography image (b) of a FeSe/TiO_2 bilayer grown on LAO substrate. (c) Atomically resolved STM topography of the same FeSe/TiO_2 bilayer.

in figure 11) ruled out the presence of both droplets and spurious domains at the surface of bilayered heterostructures. The measured RMS roughness values of the bilayers are about 0.55 nm, i.e. equivalent to the unit cell height of the FeSe. In particular, atomically resolved STM topography (panel (c) in figure 11) did show the expected in-plane squared coordination of the Fe atoms at the surface of FeSe/TiO_2 bilayer. Therefore, together with the LEED diffraction spots and STM topography investigations reveals that the overall surface quality of the FeSe/TiO_2 bilayer are equally comparable with the individual FeSe layer. The ensemble of the structural data does provide evidence of the very high quality of the FeSe/TiO_2 bilayer grown by PLD within a single-run deposition process.

6. Conclusions

In conclusion, we have reported the successful growth of both oxides and non-oxides epitaxial thin films by PLD using a Nd:YAG pulsed laser source. Differently from the literature, the fundamental emission at 1064 nm was used for growing iron selenide FeSe as well as anatase titanium dioxides TiO_2 thin films. With respect to conventional PLD based on using excimer KrF UV-lasers, the optimal growth conditions were obtained by substantially increasing the target-to-substrate distance to about 10 cm. By exploiting the flexibility and compatibility of oxide/non-oxide materials in the same PLD growth system, bilayers of epitaxial FeSe/TiO_2 were successfully deposited in a continuous deposition process. *In-situ* STM topography of the as grown FeSe/TiO_2 bilayers did show an atomically flat surface without droplets and/or undesired spurious crystallographic phases or orientation. The results show that Nd:YAG laser based PLD adds to the unique flexibility of the technique also for fabricating multiple heterostructures of very high quality, and the compactness and compatibility with *in-situ* surface analysis setups.

Acknowledgments

This work is performed in the framework of the Nanoscience Foundry and Fine Analysis (NFFA-MIUR Italy Progetti Internazionali) facility. DM and PR acknowledge the receipt of a fellowship from the ICTP Programme for Training and Research in Italian Laboratories, Trieste, Italy.

ORCID iDs

S K Chaluvadi https://orcid.org/0000-0002-3689-3336
D Mondal https://orcid.org/0000-0001-5422-7444
C Bigi https://orcid.org/0000-0003-0977-3993
D Knez https://orcid.org/0000-0003-0755-958X
P Rajak https://orcid.org/0000-0002-8728-7459
R Ciancio https://orcid.org/0000-0003-1739-3763
J Fujii https://orcid.org/0000-0003-3208-802X
G Panaccione https://orcid.org/0000-0003-0122-4041
I Vobornik https://orcid.org/0000-0001-9957-3535

G Rossi https://orcid.org/0000-0002-9330-7436
P Orgiani https://orcid.org/0000-0002-1082-9651

References

[1] Tokura Y, Kawasaki M and Nagaosa N 2017 Emergent functions of quantum materials *Nat. Phys.* **13** 1056–68
[2] Hwang H Y, Iwasa Y, Kawasaki M, Keimer B, Nagaosa N and Tokura Y 2012 Emergent phenomena at oxide interfaces *Nat. Mater.* **11** 103–13
[3] Tarancón A and Pryds N 2019 Functional oxide thin films for advanced energy and information technology *Adv. Mater. Interfaces* **6** 1900990
[4] Schlom D G, Chen L Q, Pan X, Schmehl A and Zurbuchen M A 2008 A thin film approach to engineering functionality into oxides *J. Am. Ceram. Soc.* **91** 2429–54
[5] Mbam S O, Nwonu S E, Orelaja O A, Nwigwe U S and Gou X F 2019 Thin-film coating; historical evolution, conventional deposition technologies, stress-state micro/nano-level measurement/models and prospects projection: a critical review *Mater. Res. Express* **6** 122001
[6] Schneider C W and Lippert T 2010 *Laser Processing of Materials: Fundamentals, Applications and Developments* (Berlin: Springer) pp 89–112
[7] Norton D P 2007 *Pulsed Laser Deposition of Complex Materials: Progress Toward Applications in Pulsed Laser Deposition of Thin Film: Applications-Led Growth of Functional Materials* (New York: Wiley) pp 1–31
[8] Singh R K and Narayan J 1990 Pulsed-laser evaporation technique for deposition of thin films: physics and theoretical model *Phys. Rev.* B **41** 8843–59
[9] Willmott P R and Huber J R 2000 Pulsed laser vaporization and deposition *Rev. Mod. Phys.* **72** 315–28
[10] Norton D P 2004 Synthesis and properties of epitaxial electronic oxide thin-film materials *Mater. Sci. Eng.* R **43** 139–247
[11] Coll M *et al* 2019 Towards oxide electronics: a roadmap *Appl. Surf. Sci.* **482** 1–93
[12] Delmdahl R and Pätzel R 2008 Pulsed laser deposition with excimer lasers *Phys. Status Solidi Curr. Top. Solid State Phys.* **5** 3276–9
[13] Shimizu R, Sugiyama I, Nakamura N, Kobayashi S and Hitosug T 2018 Pulsed laser deposition of oxide thin films by the fifth harmonics of a Nd:$Y_3Al_5O_{12}$ (Nd:YAG) laser *AIP Adv.* **8** 095101
[14] Orgiani P, Ciancio R, Galdi A, Amoruso S and Maritato L 2010 Physical properties of $La_{0.7}Ba_{0.3}MnO_{3-\delta}$ complex oxide thin films grown by pulsed laser deposition technique *Appl. Phys. Lett.* **96** 032501
[15] See www.trieste.nffa.eu for more information about the NFFA-APE facility
[16] Yang N, Knez D, Vinai G, Torelli P, Ciancio R, Orgiani P and Aruta C 2020 Improved structural properties in homogeneously doped $Sm_{0.4}Ce_{0.6}O_{2-\delta}$ epitaxial thin films: high doping effect on the electronic bands *ACS Appl. Mater. Interfaces* **12** 47556
[17] Gobaut B *et al* 2017 Role of oxygen deposition pressure in the formation of Ti defect states in TiO_2(001) anatase thin films *ACS Appl. Mater. Interfaces* **9** 23099–106
[18] Bigi C *et al* 2020 Direct insight into the band structure of $SrNbO_3$ *Phys. Rev. Mater.* **4** 025006
[19] Yang N *et al* 2017 Effects of dopant ionic radius on cerium reduction in epitaxial cerium oxide thin films *J. Phys. Chem.* C **121** 8841–9
[20] Amoruso S, Aruta C, Bruzzese R, Maccariello D, Maritato L, Miletto Granozio F, Orgiani P, Scotti di Uccio U and Wang X 2010 Optimization of $La_{0.7}Ba_{0.3}MnO_{3-\delta}$ complex oxide laser ablation conditions by plume imaging and optical emission spectroscopy *J. Appl. Phys.* **108** 043302
[21] Stewart G R 2011 Superconductivity in iron compounds *Rev. Mod. Phys.* **83** 1589–652
[22] Coldea A I and Watson M D 2018 The key ingredients of the electronic structure of FeSe *Annu. Rev. Condens. Matter Phys.* **9** 125–46
[23] Sakoda M, Iida K and Naito M 2018 Recent progress in thin-film growth of Fe-based superconductors: superior superconductivity achieved by thin films *Supercond. Sci. Technol.* **31** 093001
[24] Liu C and Wang J 2020 Heterostructural one-unit-cell FeSe/$SrTiO_3$: from high-temperature superconductivity to topological states *2D Mater.* **7** 022006
[25] Huang D and Hoffman J E 2017 Monolayer FeSe on $SrTiO_3$ *Annu. Rev. Condens. Matter Phys.* **8** 311–36
[26] Watson M D *et al* 2015 Emergence of the nematic electronic state in FeSe *Phys. Rev.* B **91** 155106
[27] Feng Z *et al* 2018 Tunable critical temperature for superconductivity in FeSe thin films by pulsed laser deposition *Sci. Rep.* **8** 4039
[28] Liu D *et al* 2012 Electronic origin of high-temperature superconductivity in single-layer FeSe superconductor *Nat. Commun.* **3** 931
[29] Lee J J *et al* 2014 Interfacial mode coupling as the origin of the enhancement of T_c in FeSe films on $SrTiO_3$ *Nature* **515** 245–8
[30] Ding H, Lv Y F, Zhao K, Wang W L, Wang L, Song C L, Chen X, Ma X C and Xue Q K 2016 Temperature superconductivity in single-unit-cell FeSe films on anatase TiO_2 (001) *Phys. Rev. Lett.* **117** 067001
[31] Greenfield J T, Kamali S, Lee K and Kovnir K 2015 A Solution for solution-produced β-FeSe: elucidating and overcoming factors that prevent superconductivity *Chem. Mater.* **27** 588
[32] Orgiani P *et al* 2017 Structural and electronic properties of Bi_2Se_3 topological insulator thin films grown by pulsed laser deposition *Appl. Phys. Lett.* **110** 171601
[33] Bigi C, Nardi A, Troglia A, Fujii J, Panaccione G, Vobornik I and Rossi G 2019 Robustness of topological states in Bi_2Se_3 thin film grown by pulsed laser deposition on (001)-oriented $SrTiO_3$ perovskite *Appl. Surf. Sci.* **473** 190–3
[34] Windt D L 1998 IMD—software for modeling the optical properties of multilayer films *Comput. Phys.* **12** 360
[35] Siew W O, Lee W K, Wong H Y, Yong T K, Yap S S and Tou T Y 2010 Investigation of droplet formation in pulsed Nd:YAG laser deposition of metals and silicon *Appl. Phys.* A **101** 627–32
[36] Lu D, Vishik I M, Yi M, Chen Y, Moore R G and Shen Z X 2012 Angle-resolved photoemission studies of quantum materials *Annu. Rev. Condens. Matter Phys.* **3** 129–67
[37] Damascelli A, Hussain Z and Shen Z X 2003 Angle-resolved photoemission studies of the cuprate superconductors *Rev. Mod. Phys.* **75** 473–541
[38] Yi M, Zhang Y, Shen Z X and Lu D 2017 Role of the orbital degree of freedom in iron-based superconductors *npj Quantum Mater.* **2** 57
[39] Hashimoto T *et al* 2018 Superconducting gap anisotropy sensitive to nematic domains in FeSe *Nat. Commun.* **9** 282
[40] Christen H M and Eres G 2008 Recent advances in pulsed-laser deposition of complex oxides *J. Phys. Condens. Matter* **20** 264005
[41] Koster G, Blank D H A and Rijnders G A J H M 2020 Oxygen in complex oxide thin films grown by pulsed laser deposition: a perspective *J. Supercond. Nov. Magn.* **33** 205–12

[42] Park D S *et al* 2020 The emergence of magnetic ordering at complex oxide interfaces tuned by defects *Nat. Commun.* **11** 3650

[43] Chen Y *et al* 2015 Creation of high mobility two-dimensional electron gases via strain induced polarization at an otherwise nonpolar complex oxide interface *Nano Lett.* **15** 1849–54

[44] Orgiani P *et al* 2020 Tuning the optical absorption of anatase thin films across the visible-to-near-infrared spectral region *Phys. Rev. Appl.* **13** 044011

[45] Golalikhani M *et al* 2018 Nature of the metal-insulator transition in few-unit-cell-thick $LaNiO_3$ films *Nat. Commun.* **9** 2206

[46] Orgiani P, Aruta C, Balestrino G, Born D, Maritato L, Medaglia P G, Stornaiuolo D, Tafuri F and Tebano A 2007 Direct measurement of sheet resistance $R_\square$ in cuprate systems: evidence of a fermionic scenario in a metal-insulator transition *Phys. Rev. Lett.* **98** 036401

[47] Wang Z *et al* 2017 Atomically precise lateral modulation of a two-dimensional electron liquid in anatase TiO_2 thin films *Nano Lett.* **17** 2561–7

[48] Dhaka R S *et al* 2015 Tuning the metal-insulator transition in $NdNiO_3$ heterostructures via Fermi surface instability and spin fluctuations *Phys. Rev.* B **92** 035127

[49] Knez D, Dražić G, Chaluvadi S K, Orgiani P, Fabris S, Panaccione G, Rossi G and Ciancio R 2020 Unveiling oxygen vacancy superstructures in reduced anatase thin films *Nano Lett.* **20** 6444–51

[50] Ciancio R, Carlino E, Aruta C, Maccariello D, Miletto Granozio F and Scotti Di Uccio U 2012 Nanostructure of buried interface layers in TiO_2 anatase thin films grown on $LaAlO_3$ and $SrTiO_3$ substrates *Nanoscale* **4** 91–4

[51] Ciancio R, Carlino E, Rossi G, Aruta C, Scotti Di Uccio U, Vittadini A and Selloni A 2012 Magnéli-like phases in epitaxial anatase TiO_2 thin films *Phys. Rev.* B **86** 104110

[52] Bigi C *et al* 2020 Distinct behavior of localized and delocalized carriers in anatase TiO_2 (001) during reaction with O_2 *Phys. Rev. Mater.* **4** 025801